

## Review of magnetoelectric perovskite–spinel self-assembled nano-composite thin films

Li Yan · Yaodong Yang · Zhiguang Wang ·  
Zengping Xing · Jiefang Li · D. Viehland

Received: 28 March 2009 / Accepted: 10 June 2009 / Published online: 7 July 2009  
© Springer Science+Business Media, LLC 2009

**Abstract** Two-phase multiferroic nano-composite thin films have been a topic of research interests in the last few years. This is because of their expected magnetoelectric coupling, as well as potential applications. This review focuses on recent findings in self-assembled nano-structure composite thin films, and various efforts to realize and improve their magnetoelectricity. Topics include: (i) nanopillar and maze structures, and their formation mechanisms, and a nano-belt structure oriented in-plane found by our research group; (ii) the ferroelectric properties of composite thin films, and how they can be enhanced by epitaxial engineering; (iii) a magnetic anisotropy that is induced by constraint stress, and by the nano-structures of the ferromagnetic phase; and (iv) a magnetoelectric coupling that was first observed via a change in magnetization near the Curie temperature of the ferroelectric phase, a magnetization switching assisted by electric field, and recently direct measurements using a magnetic cantilever method yielding values of 18 mV/cm Oe in  $\text{BiFeO}_3\text{-CoFe}_2\text{O}_4$ .

### Introduction

Multiferroics are materials that have more than one primary ferroic order parameter. The term multiferroic was first used by Schmid [1], which initially only referred to single-phase materials, but was later expanded to include any material that had two or more types of long-range spontaneous (magnetic, ferroelectric, and/or ferroelastic)

orderings. An early and important type of multiferroic was magnetoelectric (ME) materials, which possessed both ferromagnetic and ferroelectric orderings.

Single-phase ME effects were first reported in  $\text{Cr}_2\text{O}_3$  in 1961 [2, 3] which stimulated much research in the 1960s and 1970s. However, these single-phase multiferroic materials only had coexisting order parameters at low temperatures, and in addition their magnetoelectric (ME) responses were generally very weak. These problems languished the research field of magnetoelectricity until the emergence of composites, which yielded giant magnetoelectric coefficients at room temperature via an interaction of elastic strain between ferroelectric and ferri-/ferromagnetic phases. Scientific interest in the physical properties of these composites, in addition to great potential for applications (as actuators, switches, magnetic field sensors, or new types of electronic memory devices) has resulted in magnetoelectric materials receiving significant research interests during recent years, especially as thin films [4, 5].

Composite thin film multiferroic materials can generally be divided into three types: (i) a 0-3 structure, which is generally a magnetoelastic material embedded in a piezoelectric matrix (i.e.,  $\text{CoFe}_2\text{O}_4$  or CFO nanoparticles in a  $\text{Pb}(\text{Zr},\text{Ti})\text{O}_3$  or PZT matrix); (ii) a 2-2 structure, which is generally multilayer thin films of magnetostrictive and piezoelectric materials; and (iii) a 1-3 structure, such as monolayer self-assembled nanostructures (i.e., CFO nanopillars in a  $\text{BiFeO}_3$  or BFO matrix).

Magnetoelectric composites with a 0-3 phase interconnectivity have been fabricated by both sol-gel [6–8] and pulsed laser deposition (PLD) [9]. Sol-gel is suitable for thicker film deposition, whereas PLD allows obtainment of thin films with better quality. CFO or  $\text{NiFe}_2\text{O}_4$  (NFO) are often used as the magnetoelastic phase in ME composites, and PZT as the piezoelectric one: each chosen for their

L. Yan (✉) · Y. Yang · Z. Wang · Z. Xing · J. Li · D. Viehland  
Department of Materials Science and Engineering,  
Virginia Tech, Blacksburg, VA 24061, USA  
e-mail: liyan@vt.edu

high magnetoelastic and piezoelectric coefficients, respectively. Ren and Wuttig [10] modified this method using sol–gel to deposit CFO/Fe<sub>3</sub>O<sub>4</sub> nanoparticles on Pb(Mg<sub>1/3</sub>Nb<sub>2/3</sub>)O<sub>3</sub>–PbTiO<sub>3</sub> or PMN-PT single crystal substrates, which served both as substrate and strain mediator. The ME coupling coefficient was measured, although it was not very high compared to bulk co-fired layered composites due to interaction between the two composite layers and the substrate (i.e., clamping).

Magnetolectric composites of a 2-2, or multilayer interconnectivity, of ferroelectric and piezoelectric phases have been deposited heteroepitaxially as thin-layers on single crystal substrates by PLD [11–15] and sol–gel [16, 17]. The advantages of this 2-2 connectivity is that it is easy to manipulate and has great application potential, but again substrate clamping effects present problems that must be overcome to achieve enhanced ME coupling coefficients. Much research has been directed toward the objectives of a high-resistance piezoelectric layer, and integration with Si.

Finally, research has focused on multiferroic monolayered self-assembled nanostructures, following the original report of Zheng et al. [5]. These researchers deposited differently shaped BiFeO<sub>3</sub>–CoFe<sub>2</sub>O<sub>4</sub> (BFO–CFO) nanostructures on variously oriented SrTiO<sub>3</sub> (STO) substrates [18, 19], and successfully realized magnetization switching under electric field assistance [20, 21]. Levin et al. [22, 23] have also deposited similar nanostructures, and combined experimental and theoretical results confirming their assertion that epitaxial growth of two immiscible phases on a single crystal substrate can occur due to elastic strain interaction between the two phases, which determines their growth dynamics and final morphology.

Monolayer self-assembled structures are believed to have good interactions between the two constituent phases, thus enhancing the ME effect. In particular, vertically aligned structures might overcome substrate clamping effects. In such nano-composite heteroepitaxial thin films, accurate property characterization of each single phase is very important in order to fully characterize and understand the composite ME effects. *In this review, we will focus on two phase self-assembled nano-composite thin films, including the nano-structure, ferroelectric, and ferromagnetic properties of both the piezoelectric and magnetoelastic phases, and magnetolectric coupling in composite thin films.*

### Nano-structures of self-assembled nano-composite thin films

Nano-structured self-assembled two-phase monolayer composite thin films are an important class of materials that can have multiferroic and magnetolectric properties: in

particular those of magnetostrictive spinel and piezoelectric perovskite. The nano-structures (i.e., distribution, size, connectivity) of each phase are important factors determining the coupling strength between the polar and spin subsystems.

#### Background: nano-rods and nano-maze

Zheng et al. [5] were the first to report self-assembled ferroelectric-ferromagnetic (1-3) nano-composite thin films: where CFO formed as nano-pillars embedded in a BTO matrix. After that, to understand the growth mechanism and improve the multi-ferroelectric properties, numerous investigations of similar systems were reported: such as those with different perovskite (BTO, BFO, PbTiO<sub>3</sub> (PTO), and PZT) and spinel (CFO and NFO) phases, different spinel/perovskite or S/P atomic ratios (1/2, 1/1, and 2/1), different substrates with different lattice parameters (LaAlO<sub>3</sub>: 3.79 Å, SrTiO<sub>3</sub>: 3.90 Å, MgAl<sub>2</sub>O<sub>4</sub>: 8.08 Å, and MgO: 4.21 Å), different substrate orientations [(001), (110), and (111)], and different film thicknesses [5, 18–30].

For all material couples, of all S/P ratios and substrates, it was found that epitaxial films had a (1-3) phase connectivity at the nm-level when deposited on the (001) orientation: spinel formed nano-pillars that were vertical to the substrate and that were embedded in a perovskite matrix; and in a (3-1) connectivity when deposited on the (111) orientation, where spinel was the matrix phase that was embedded with perovskite nano-pillars. However, for the (110) orientation, the nano-structures were more complicated: spinel changed from a nano-pillar to a nano-maze structure [23]. Zheng et al. [18] found that the reason was perovskite wets better than spinel on (001) substrates, and that spinel wets better than perovskite on (111) substrates. However, wetting could not explain why spinel preferred to form as nano-pillars on (001) spinel MgAl<sub>2</sub>O<sub>4</sub> substrates, or on CFO buffer-layers. Also it could not explain the complicated nano-structure found when deposited on (110) substrates. Slutsker et al. [22, 23, 31–33] gave an explanation based on elastic interactions: by considering each phase as an elastic domain that is under a constraint stress imposed by the substrate. Following this elastic model, not only could the (1-3) and (3-1) nano-structures on (001) and (111) substrates be explained, but also more complicated phase connectivities on (110) substrates could be too.

In the BFO–CFO system, Zheng et al. [19] used Wulffnet shapes to explain why the CFO phase formed with pyramidal structures that were embedded in a flat BFO matrix, both deposited on (001) oriented substrates. Correspondingly, BFO formed as triangular pyramids embedded in a flat CFO matrix on (111) substrates. In this case, CFO is an octahedron with eight {111} faces, and BFO is a cube with six {001} ones: this is because the (111) face of

CFO and (001) face of BFO have the lowest surface energies.

In addition to phase connectivities and crystal structures, another important factor may also influence the nano-structure of the composite thin film: that is CFO tends to elongate along the [110] direction due to a ledge growth mechanism [34]. Our research group has found CFO nano-belts in both the BTO–CFO and BFO–CFO systems [35, 36].

Nano-belts in  $\text{BaTiO}_3\text{--CoFe}_2\text{O}_4$  and  $\text{BiFeO}_3\text{--CoFe}_2\text{O}_4$  composite thin films

Composite thin films of BTO–CFO were deposited on (001) STO substrates at 1,070 K [35]. After annealing at 1,270 K, it was found that CFO crystallized as pyramids with (111) facets in the out-of-plane direction which were embedded in a BTO matrix (Fig. 1a), similar to prior reports [5, 24]. However, after the films were annealed above 1,300 K using a very slow ramp rate (40 K per step and dwell 2 h for

each step), a CFO nano-belt structure (Fig. 1b) was found that was elongated along the [110] direction. Below 1,210 K, only a small volume fraction of CFO nano-structures was observed with  $L \approx W = 60$  nm. When the temperature was increased to 1,250 K, nano-structure growth became anisotropic along the [110] with  $L = 300$  nm and  $W = 100$  nm. At 1,290 K, this anisotropic growth resulted in nano-belt dimensions of  $L = 700$  nm and  $W = 120$  nm. Annealing was ended at 1,370 K, where the CFO nano-belts had grown to  $L = 1,200$  nm and  $W = 150$  nm.

Layers of BFO–CFO composite thin films were deposited on (001), (110), and (111) STO substrates [36]. The nano-structures of these composite thin films are shown in Fig. 2a–c. Similar to BTO–CFO and other prior reports [19], CFO grown (001) STO formed as nano-pillars with a pyramidal morphology that was embedded within a BFO matrix (see Fig. 2a). Alternatively, when grown on (111) STO, CFO was the matrix phase with embedded BFO nano-pillars of triangular morphology (see Fig. 2c). However, when grown on (110) STO, CFO formed with a

**Fig. 1** Nano-structures of  $\text{BaTiO}_3\text{--CoFe}_2\text{O}_4$  (BTO–CFO) composite thin films: (a) and (b) are nano-pillar and nano-belt of BTO–CFO films, respectively [35]

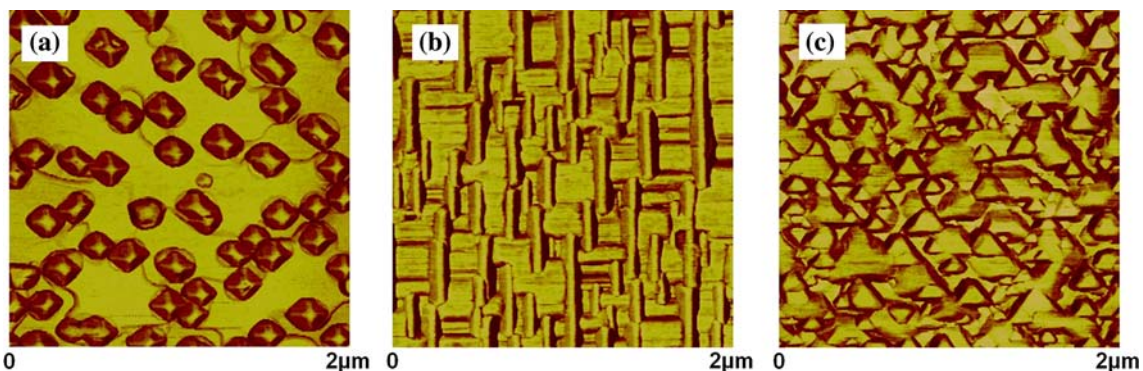
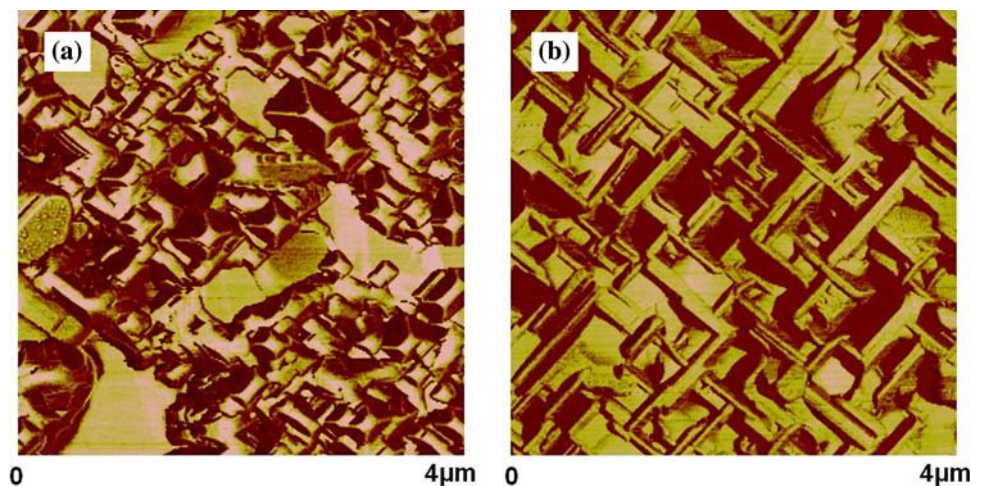


**Fig. 2** Nano-structures of  $\text{BiFeO}_3\text{--CoFe}_2\text{O}_4$  (BFO–CFO) composite thin films: (a–c) are CFO pyramidal nano-pillar, CFO nano-belt, and BFO triangle nano-pillar structures of BFO–CFO films, respectively [36]

nano-belt structure (see Fig. 2b). Again, the nano-belts are anisotropic and elongated along the  $[110]$ , with much narrower widths oriented in the  $[001]$  direction. Furthermore, films deposited at 810 K had only a small volume fraction of CFO nano-dots of size  $\sim 10$  nm. When the deposition temperature was increased to 930 K, CFO began growing anisotropically along the  $[110]$  with  $L = 130$  nm and  $W = 30$  nm. With increase of the deposition temperature, this anisotropy increased: at 1,020 K,  $L = 500$  nm and  $W = 100$  nm, with some nano-belts reaching more than 2,000 nm in length.

We also deposited films on (100), (130), (120), and (110) STO substrates: which were  $0^\circ$ ,  $18^\circ$ ,  $26^\circ$ , and  $45^\circ$  tilted away from the (100) orientation, respectively, as shown in Fig. 3a–d. In BFO–CFO films grown on a (100) substrate, CFO formed as nano-rods. In the case of films grown on substrates that were  $0^\circ$ ,  $18^\circ$ , to  $26^\circ$  tilted from the (100) orientations,  $[110]$  spinel ridges tended to form but were always truncated by translating into perovskite phase regions. However, for the (110) orientation, the  $[110]$  spinel ridges were free to extend indefinitely.

Nano-belts of CFO were found both for BTO–CFO grown on (001) STO after annealing and for BFO–CFO grown on (110) STO in the as-deposited condition. The nano-belts were elongated along the  $[110]$  in both cases. The reason for the elongation of spinel along the  $[110]$  direction is a ledge growth mechanism. Yanina and Carter [34] reported that spinel single crystals tend to grow along the  $[110]$ . Due to a special distribution of cations in spinel which occurs along the  $[110]$  direction, ledge growth of spinel tends to occur preferentially along the  $[110]$ .

### Ferroelectric properties of self-assembled nano-composite thin films

A comparison of the polarization for BFO–CFO [37] and BTO–CFO [5] nano-composites with that of single phase BFO [4] and BTO is shown in Fig. 4. It can be seen that the polarization of the ferroelectric phase is similar to that of the pure perovskite: the larger the coercive field for the pure ferroelectric material, the higher it is in the

**Fig. 3** AFM results of BFO–CFO nano-composite thin films deposited on **a** (100), **b** (130), **c** (120), and **d** (110) oriented STO substrates. The images illustrate the elongation of  $[110]$  ridges of CFO nano-belts [36]

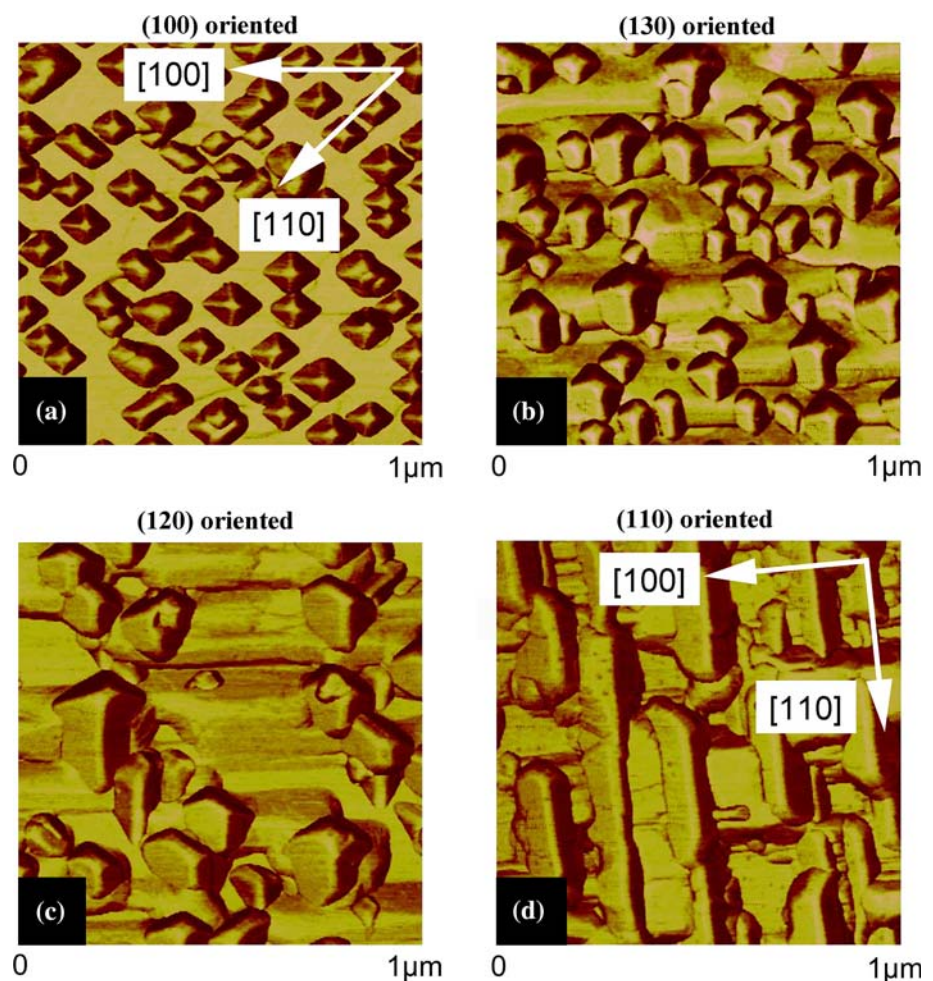
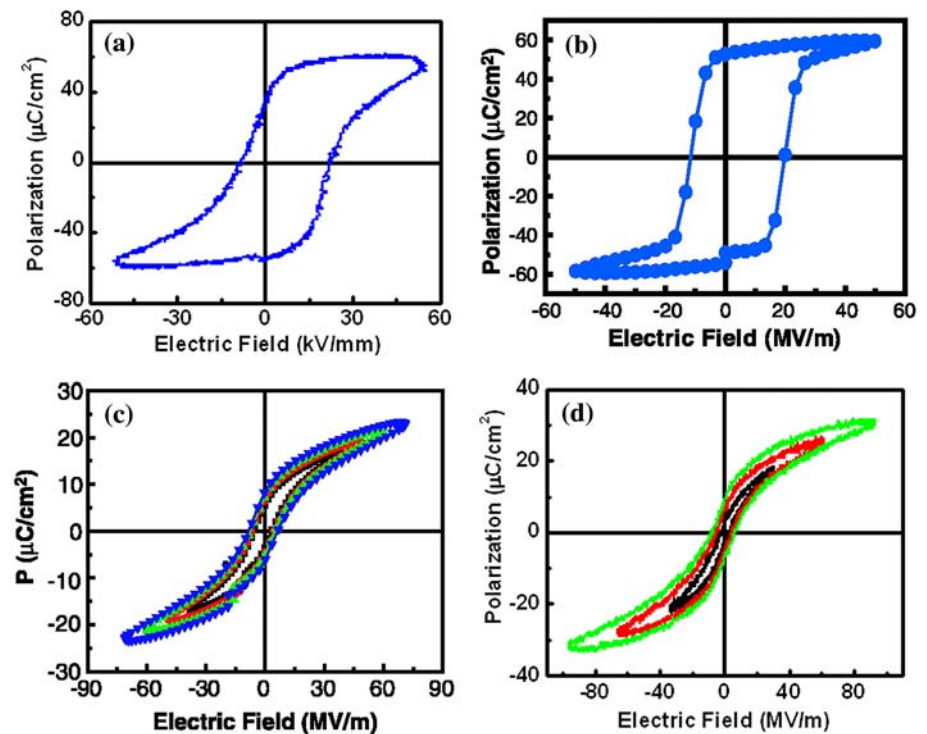


**Fig. 4** P–E hysteresis loops of **a** BFO–CFO self-assembled nano-composite thin film [37]; **b** BFO thin film [4]; **c** BTO–CFO self-assembled nano-composite thin film [5]; and **d** BTO thin film



nano-composite: also, the higher the saturation polarization in the pure FE phase, the higher it is in the nano-composite. From this comparisons, we can see that to improve the ferroelectric properties of self-assembled nano-composite thin films, it is necessary to exploit the ferroelectric properties of single phase ferroelectric materials. The better the properties of the perovskite phase, the better the properties of the nano-composite.

### Background

Compared with bulk materials, thin films have constraint stresses imposed from the substrate which may notably change the structure and properties of the thin films. There are numerous reasons why a constraint stress can be generated between thin films and substrates: such as different thermal expansion coefficients, cooling rates, external electric fields, stresses induced by the growth process, and etc. In all of these cases, the stress generated by lattice mismatch is the most important factor for epitaxial thin films [38]. Stress can also be applied by an elastic bending of the substrate, during deposition and annealing [39, 40].

The constraint stress of the thin film may be relaxed by increasing the thickness of the film. The critical thickness can be estimated by the Matthew–Blakeslee (or mechanical equilibrium) model, or by the People–Bean (or energy equilibrium) model [41–43]. Due to the relaxation of the compressive stress with increase of the film thickness, the lattice parameters ( $c$  and  $a$ ) consequently decrease with

increasing thickness. The polarization of tetragonal ferroelectrics decreases with decreasing film thickness, due to compressive stresses, as observed for BTO, PTO, and PZT [44–50].

For these tetragonal ferroelectrics, such as BTO, PTO, and PZT, the constraint stress is also able to alter their domain structures. There are three types of ferroelectric domains for tetragonal films, or combinations thereof:  $a_1$ ,  $a_2$ , and  $c$  which represent the lattice constant  $c$  is oriented along the  $x$  (in-plane),  $y$  (in-plane), and  $z$  (out-of-plane) directions, respectively [51]. Generally, when the stress changes from tensile to compressive, the volume ratio of the  $c$  domains increases [52–54]. Specifically, Alpay and Roytburd [52] have calculated domain structures for tetragonal ferroelectrics, and determined how the domain distribution changes with stress. Experimental findings for PTO and BTO agreed with their predictions. With increase of the  $c$  domain population, the polarization of the thin films was increased: this is simply because the polarization was measured in the out-of-plane direction.

Compressive stresses may also increase the ferroelectric Curie temperature, and the  $c/a$  ratio of tetragonal thin films. Choi et al. [55] selected  $\text{DdScO}_3$  and  $\text{DyScO}_3$  as substrates, which have lattice mismatches of  $-1.0$  and  $-1.7\%$  with BTO thin films, respectively. They found that the Curie temperature of BTO increased from  $130$  to  $400$  °C for the  $\text{DdScO}_3$  substrate, and to  $540$  °C for the  $\text{DyScO}_3$  one. Correspondingly, the  $c/a$  ratio of BTO increased from  $1.011$  to  $1.026$  for the  $\text{DdScO}_3$  substrate, and  $1.039$  for

DyScO<sub>3</sub>. Furthermore, the polarization of BTO on DyScO<sub>3</sub> was 2.7 times higher than that of BTO single crystals.

By changing the orientation of the substrate, the direction of the constraint stress can be varied. Thus, the crystal structure of the perovskite phase may be different on variously oriented substrates/buffer-layers, resulting in a change of ferroelectric properties. Accordingly, the topic which we will discuss below is the relationship among the substrate orientations, crystal structures, lattice parameters, and ferroelectric properties.

Phase engineering of perovskite materials

*Enhanced ferroelectric properties of Pb(Zr<sub>1-x</sub>Ti<sub>x</sub>)O<sub>3</sub> thin film in low symmetry phase*

Lead zirconium titanate, Pb(Zr<sub>1-x</sub>Ti<sub>x</sub>)O<sub>3</sub> or PZT, is a widely used ferroelectric material. From the phase diagram, it can be observed that a morphotropic phase boundary (MPB) is located near  $x = 0.48$  at room temperature. For  $x < 0.48$ , the stable phase has a rhombohedral (R) structure; whereas for  $x > 0.48$ , it is tetragonal (T) [56]. Furthermore in 1999, a new monoclinic M<sub>c</sub> phase was reported in the MPB region of bulk PZT ceramics by neutron diffraction [57].

Epitaxial thin films of Pb(Zr<sub>0.52</sub>Ti<sub>0.48</sub>)O<sub>3</sub> have been deposited on (001), (110), and (111) SrTiO<sub>3</sub> substrates [58]. The composition of PZT was chosen to be right at the MPB. The PZT thin films were found to have T, M<sub>c</sub>, and R structures when deposited on (001), (110), and (111) oriented SrTiO<sub>3</sub> substrates, respectively. The room temperature lattice constants of (001), (110), and (111) PZT thin films were ( $a_t, c_t$ ) = (4.044, 4.132 Å), ( $a_m, b_m, c_m, \beta_m$ ) = (4.059, 4.049, 4.098 Å, 90.44°), and ( $a_r, \alpha_r$ ) = (4.017 Å, 89.58°), respectively.

Figure 5a can be used to explain the different crystal structures for the variously orientated substrates. The

composition of PZT was at the MPB region, which can be either T or R. The in-plane compressive constraint stress between an epitaxial thin film and a (001) substrate is tensile along [001] and normal to the (001) plane: such a stress favors films with a stable T structure. Whereas, an in-plane compressive stress along (111) results in a tensile stress along [111]: favoring a stable R structure. This constraint stress can extend phase stability regions past the conventional MPB. In fact, prior investigations have reported that a T phase can be stable until  $x = 0.4$  on (001) STO, whereas the R phase can be stable until  $x = 0.6$  on (111) STO [59]. On (110) STO, although the stress is along [110], there is no stable O phase in PZT: combination of a stable T phase with stress along [110] results in a monoclinic M<sub>c</sub> structure for PZT grown on (110) STO.

The polarizations of PZT thin films grown on different orientations of STO are shown in Fig. 5b. It can be seen that the saturation polarization of (001), (111), and (110) PZT are 0.9, 1.1, and 1.3 C/m<sup>2</sup>, respectively. The saturation polarization of the films followed the general trend of M<sub>c</sub> > R > T. The polarization of the M<sub>c</sub> phase was higher than that of the R or T ones. By changing the crystal structure of PZT via substrate orientation, the ferroelectric properties can be enhanced: with the highest values occurring in the M<sub>c</sub> structure.

*Stress-enhanced multiferroic properties of Pb(Fe<sub>1/2</sub>Nb<sub>1/2</sub>)O<sub>3</sub> thin films*

Lead iron niobate, Pb(Fe<sub>1/2</sub>Nb<sub>1/2</sub>)O<sub>3</sub> or PFN, is a relaxor ferroelectric below its Curie temperature of  $T_C \approx 393$  K [60–62]. On cooling, PFN undergoes a transformation sequence of C → T → R. The T phase only exists over a narrow temperature range of 40 K below  $T_C$ . At room temperature, PFN has a stable R phase with lattice constants of  $a_r = 4.012$  Å and  $\alpha_r = 89.89^\circ$ , which are nearly pseudo-cubic [63–66].

**Fig. 5** Structure and ferroelectric properties of Pb(Zr<sub>0.52</sub>Ti<sub>0.48</sub>)O<sub>3</sub> (PZT) thin films deposited on (001), (110), and (111) SrTiO<sub>3</sub> (STO) substrates. **a** Illustration of where polarization direction lies for the T, M<sub>c</sub>, and R phases of PZT deposited on (001), (110), and (111) STO; and **b** P–E hysteresis loops of M<sub>c</sub>, R, and T PZT films [58]

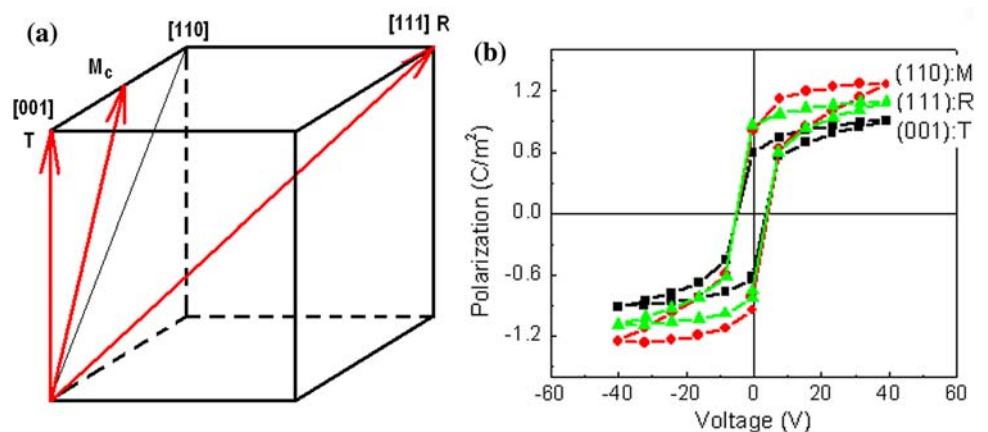
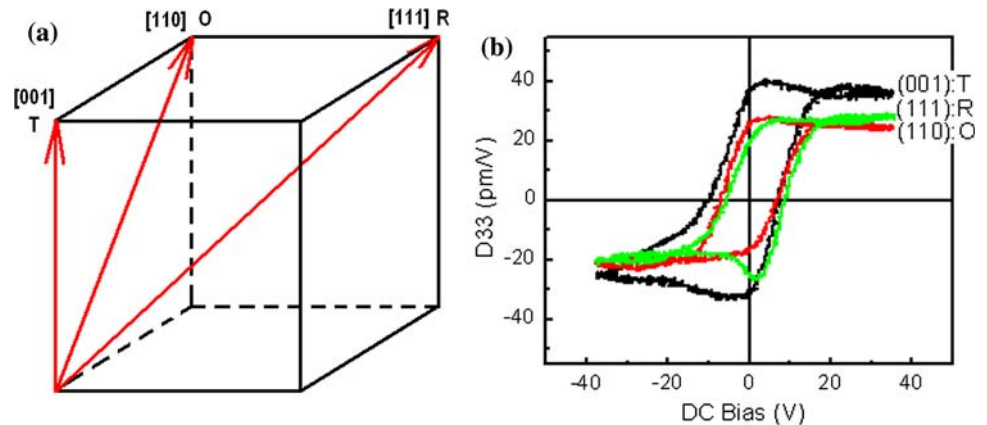


**Fig. 6** Structure and ferroelectric properties of  $\text{Pb}(\text{Fe}_{0.5}\text{Nb}_{0.5})\text{O}_3$  (PFN) thin films deposited on (001), (110), and (111)  $\text{SrTiO}_3$  (STO) substrates. **a** Illustration of where polarization direction lies for the T, O, and R phases of PFN deposited on (001), (110), and (111) STO; and **b** P–E hysteresis loops of T, R, and O phases of PFN layers [69]



Thin films of PFN deposited on (001), (110), and (111) STO substrates have stable T, O, and R phases with lattice constants of  $(a_t, c_t) = (4.010, 4.068 \text{ \AA})$ ,  $(a_o/\sqrt{2}, b_o/\sqrt{2}, c_o) = (4.032, 4.026, 4.017 \text{ \AA})$ , and  $(a_r, \alpha_r) = (4.027 \text{ \AA}, 89.96^\circ)$ , respectively [67, 68]. Figure 6a is used to explain why PFN has different stable phases on differently oriented substrates. On (111) STO, PFN has a stable R phase because of an equivalent tensile stress along the [111] direction imposed by the substrate. On (001) STO, the stable phase is T due to an equivalent tensile stress along [001]. In PFN crystals, the T phase is stable only over the temperature range of 353–393 K: the constraint stress increases this temperature stability range of the T phase notably, such that it is stable at room temperature. On (110) STO the stable phase is O. This is because PFN crystals at room temperature are nearly pseudo-cubic, without notable distortions: thus, the constraint stress from the (110) substrate compresses it to orthorhombic (O).

The piezo-responses of the variously oriented PFN thin films are shown in Fig. 6b [69]. It can be observed that the T phase has a higher  $d_{33}$  value (40 pm/V), than either the R or O phases (26 pm/V). The higher piezo-response of the T phase may be induced by the stronger constraint stress from the substrate. From calculations, we found that the constraint stress from the (001) STO substrate was more than  $10\times$  larger than that of (110) or (111) STO. The higher constraint stress from the (001) substrate results in the T phase of PFN being more strongly distorted from the pseudo-cubic, than films grown on (111) or (110).

#### Triclinic phase in $\text{BiFeO}_3$ thin films

Bismuth ferrite,  $\text{BiFeO}_3$  or BFO, is also ferroelectric below a  $T_C = 1,103 \text{ K}$  [70–74]. On cooling, BFO crystals undergo a transformation sequence of  $C \rightarrow R$ . At room temperature, BFO crystals and ceramics have a stable R phase with lattice constants of  $a_r = 4.012 \text{ \AA}$  and  $\alpha_r = 89.89^\circ$ , which again is nearly pseudo-cubic [70, 71, 75–79]. Thin films of BFO deposited on (001), (110), and

(111) STO substrates have stable monoclinic  $M_a$ , monoclinic  $M_b$ , and R phases, respectively [80–82].

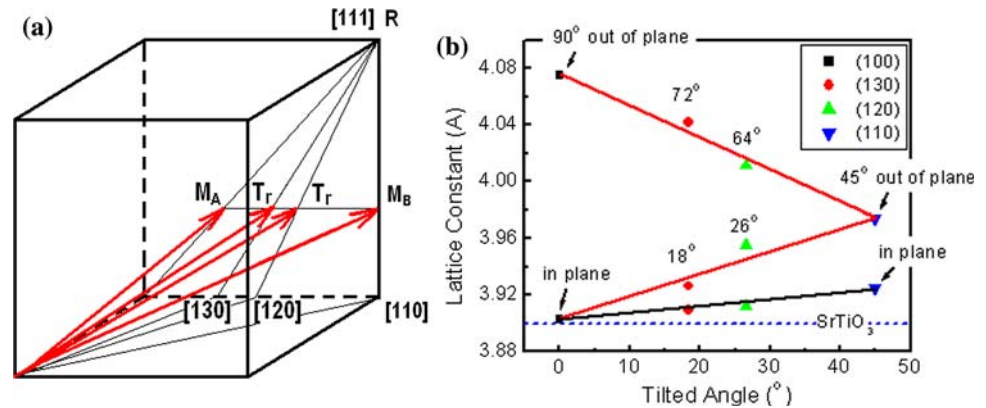
Films of BFO deposited on (100), (130), (120), and (110) STO substrates have been investigated by XRD: resulting in stable  $M_a$ , triclinic, triclinic, and  $M_b$  phases with lattice constants of  $(a_M/\sqrt{2}, b_M/\sqrt{2}, c_M, \beta) = (3.919, 3.887, 4.075 \text{ \AA}, 89.34^\circ)$ ,  $(a_{tr}, b_{tr}, c_{tr}; \alpha_{tr}, \beta_{tr}, \gamma_{tr}) = (3.926, 4.041, 3.909 \text{ \AA}, 89.52^\circ, 89.51^\circ, 89.30^\circ)$ ,  $(a_{tr}, b_{tr}, c_{tr}; \alpha_{tr}, \beta_{tr}, \gamma_{tr}) = (3.955, 4.011, 3.912 \text{ \AA}, 89.52^\circ, 89.51^\circ, 89.34^\circ)$  and  $(a_M/\sqrt{2}, b_M/\sqrt{2}, c_M, \beta) = (3.996, 3.952, 3.925 \text{ \AA}, 89.24^\circ)$ , respectively [80]. Figure 7a illustrates why these different phases are stable when deposited on the variously oriented STO substrates. The stable phase of bulk BFO is R. The combination of this R phase with an equivalent stress along [100], [130], [120], and [110] distorts the stable phase to being  $M_a$ ,  $t_r$ ,  $t_r$ , and  $M_b$ , respectively.

In Fig. 7b, we show the relationship between the lattice constants of (100), (130), (120), and (110) for BFO as a function of the tilt angle between the substrate's surface and the (100). In this figure, it can be seen that the lattice parameters are near linearly dependent on the tilt angle. The in-plane lattice constants range in values from 3.90 to 3.92  $\text{\AA}$ , with little difference induced by the asymmetry of in-plane stresses on tilted (100) substrates. With the increase of the tilt angle, the range of lattice constants increased from between 3.90 and 4.08  $\text{\AA}$ . This data shows by selecting properly oriented substrates that it is possible to engineer lattice constants of low symmetry phases to particular desired values.

#### Summary

By selecting the orientation of substrates, it is possible to change the crystal structures and lattice constants of ferroelectric thin films of PZT, PFN, and BFO. This is due to strong in-plane compressive constraint stresses between the epitaxial thin film and the single crystal substrate. The constraint stress can (i) alter the phase stability even when

**Fig. 7** Structure and lattice parameters of BiFeO<sub>3</sub> (BFO) thin films deposited on (100), (130), (120), (110), and (111) SrTiO<sub>3</sub> (STO) substrates. **a** Illustration of where the polarization direction has forth M<sub>A</sub>, T<sub>r</sub>, T<sub>r</sub>, M<sub>B</sub>, and R phases of BFO deposited on (100), (130), (120), (110), and (111) STO; and **b** lattice parameters of BFO films on (100), (130), (120), and (110) STO [80]



the composition is crossed over the original MPB of bulk PZT; (ii) enhance the phase stability to temperatures notably lower than the corresponding bulk PFN; and (iii) stabilize low symmetry monoclinic and triclinic structures which are non-existent in bulk BFO. Our findings show that off-axis substrates can be used to engineer bridging phases of the lowest possible symmetry. Such low symmetry phases may be important to enhance piezoelectric properties. In particular, for magnetoelectric composites, the ability to tune the symmetry of the matrix of the piezoelectric coefficients offers an important approach to controlling product tensor properties.

### Ferromagnetic properties of self-assembled nano-composite thin films

Another important property of self-assembled nano-composite thin films is ferromagnetism. Detailed investigations of the effect of said nano-structures, or other factors, on the ferromagnetic properties are quite interesting and will be discussed below.

#### Background

It was reported that CFO nano-pillars embedded in a BTO matrix have strongly anisotropic magnetic properties [5]. The M–H curve measured in the out-of-plane direction is square with relatively large coercive fields (5 kOe) that saturate quickly on further increase of H (10 kOe). However, the magnetization along the in-plane direction is slim loop, with a small coercive field (1 kOe) that saturates much more slowly with increasing H (50 kOe). After comparing the magnetic anisotropy of CFO nano-pillar structures prepared at different deposition temperatures, Zheng et al. [5, 83] found that this anisotropy was induced by the constraint stress of the heterostructure. With increase of deposition temperature, this magnetic anisotropy was found to decrease [83].

Recent investigations have revealed a relationship between the magnetic anisotropy and the height/diameter ratio of NFO nano-pillars [84]. It was found with increasing film thickness that the height of the NFO nano-pillars increased: as a result, the aspect ratio obviously also increased. The magnetic anisotropy is strongly related to the aspect ratio of the spinel phase. For thinner films (1:2 aspect ratio for NFO), the M–H curves in the in-plane and out-of-plane directions were almost the same; but for thicker films (10:1 aspect ratio for CFO), the M–H curve for in-plane was much slimmer and harder to saturate, relative to out-of-plane.

Not only can nano-pillars with out-of-plane orientations be deposited, but our research group has found that nano-belts elongated along in-plane directions can also be deposited. This makes it possible to study the relationship between various nano-structures and magnetic behaviors.

#### Ferromagnetic properties of CoFe<sub>2</sub>O<sub>4</sub> nano-pillars, nano-belts, and matrix

The magnetization hysteresis loops for a CFO single layer, a nano-pillar one oriented in the out-of-plane direction, and a nano-belt one oriented along the [110] are shown in Fig. 8a [35]. The M–H curve for the CFO single layer was a standard hysteresis loop, where it was easy to rotate the spin and achieve a relatively high remnant magnetization. For CFO nano-pillar structures, it was harder to saturate the magnetization along the in-plane direction than it was for a single layer. This was because the nano-pillars are oriented out-of-plane, and thus it is difficult to rotate their spin toward the in-plane direction. Furthermore, on removal of the magnetic field, the remnant magnetization was notably lower than that for a CFO single layer: this is because it is difficult to maintain the magnetization to lie out-of-plane. In the case of CFO nano-belt structures, the belt was elongated along the [110] with its width normal to that direction. The geometrical shape factor  $L/W$  was  $\sim 10$ , which was much larger than the height/width ratio of the



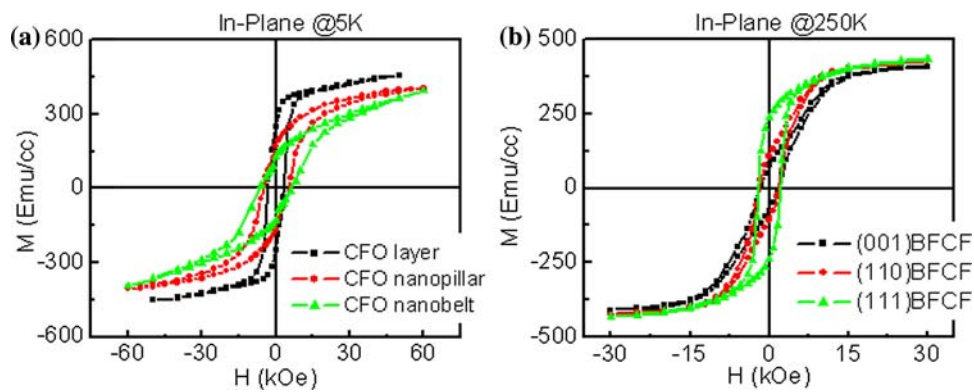


**Fig. 8** **a** M–H loops of CFO single layer, CFO nano-pillar, and CFO nano-belt, demonstrating the relationship between nano-structures and magnetic properties of BTO–CFO films [35]; and **b** M–H loops of

(001), (110), and (111) oriented BFO–CFO composite films, demonstrating the relationship between nano-structures and magnetic properties of BFO–CFO films [36]

nano-pillar structure. Accordingly, its magnetization was the hardest to saturate under external magnetic field, and it has the lowest remnant magnetization.

The in-plane ferromagnetic hysteresis loops for (001), (110), and (111) oriented layers are shown in Fig. 8b [36]. The wetting of CFO on STO follows the general trend of (111) > (110) > (001). Thus, CFO changed from being the matrix to being nano-belts, to being nano-pillars on (111), (110), and (001) STO, respectively. Higher wetting angles mean that the CFO spreads more readily on STO substrates. This results in reduced shape anisotropy for the CFO phase where it is easier to saturate the spins in-plane, resulting in a lower coercive field and a higher remnant magnetization. On the contrary, lower wetting of CFO on STO means that the CFO is more isolated on the substrates. This makes it more difficult to saturate the magnetization in-plane, resulting in higher coercive fields and lower remnant magnetizations. From Fig. 8d, we can clearly see that the field needed to reach saturation follows the general trend of (001) > (110) > (111); whereas that for the remnant magnetization is (111) > (110) > (001).

Clearly, the ferromagnetic properties of CFO nano-structures are strongly related to the shape of the nano-structures. This is because spin alignment and rotation are quite different for these nano-scale structures, compared to corresponding CFO thin layers.

### Magnetoelectric properties of self-assembled nano-composite thin films

The magnetoelectric properties of self-assembled nano-composite thin films are the result of a coupling between the polarization of the ferroelectric phase and the magnetization of the ferromagnetic one. Thin ME films should exhibit a change of polarization with application of external magnetic field, or a change of magnetization with electric field.

However, due to the finite size of the nano-composites, the ME signal of thin film is quite small and difficult to measure [85]. Accordingly, research of ME coupling in self-assembled nano-composite has been quite limited.

### Background

The first indication of ME coupling in self-assembled nano-composite thin films was reported for the BTO–CFO system in 2004 [5]. A kink was observed in the magnetization at the ferroelectric Curie temperature of the BTO phase. At this temperature, the BTO matrix underwent a phase transformation from cubic to tetragonal. The change in the perovskite crystal structure of the BTO matrix then resulted in a distortion of the CFO crystal structure. As a consequence, the magnetization of CFO was reduced at this temperature, via magnetostriction.

Other evidence of ME coupling has been provided by studies of electric field assisted magnetization switching using a MFM method [21]. On applying a voltage of  $-16$  V to the film and no magnetic field applied, approximately 50% of the magnetization of the CFO nano-pillars was rotated due to a ME coupling between BFO and CFO. If the film was then exposed to a magnetic field while under this voltage of  $-16$  V, the percentage of spin rotation increased with increasing DC magnetic field: up to 90% could be rotated under  $H = 800$  Oe.

There have also been several reports of ME coupling in (0-3) and (2-2) type composite thin films by other measurement methods. These include: (i) the saturation polarization being decreased from 80 to 25  $\mu\text{C}/\text{cm}^2$  when a DC magnetic field of 10 kOe was applied to (0-3) CFO–PZT thin films [86]; (ii) the ferroelectric coercive field increased from 4.8 to 6.6 MV/m under application of DC magnetic field of 5 kOe for (2-2) PZT/CFO thin films [87]; (iii) the ferromagnetic resonance frequency of yttrium iron garnet or YIG layers being increased by 5 Oe when a voltage of

25 V was applied to (Ba,Sr)TiO<sub>3</sub> or BSTO layers which were deposited on the top of the YIG one [88]; and (iv) a ME voltage output of 5 μV that was observed when a square wave AC magnetic field of 6 Oe was applied to a (2-2) NFO/BTO composite thin film [13].

Direct measurement of the magnetoelectric coefficient in CoFe<sub>2</sub>O<sub>4</sub>–BiFeO<sub>3</sub> nano-composite thin films

A magnet cantilever method has been used to measure the ME voltage output in (1-3) CFO–BFO self-assembled composite thin films [37]. Because the tiny ME voltage output in composite thin films may be buried in the noise induced from cables and environment, it was necessary to use a higher AC magnetic field to generate a higher ME voltage to make direct ME measurements possible. The measurement method is shown in Fig. 9a. The magnetic cantilever was excited by a shaker. By changing the input voltage of the shaker, the vibration amplitude of the

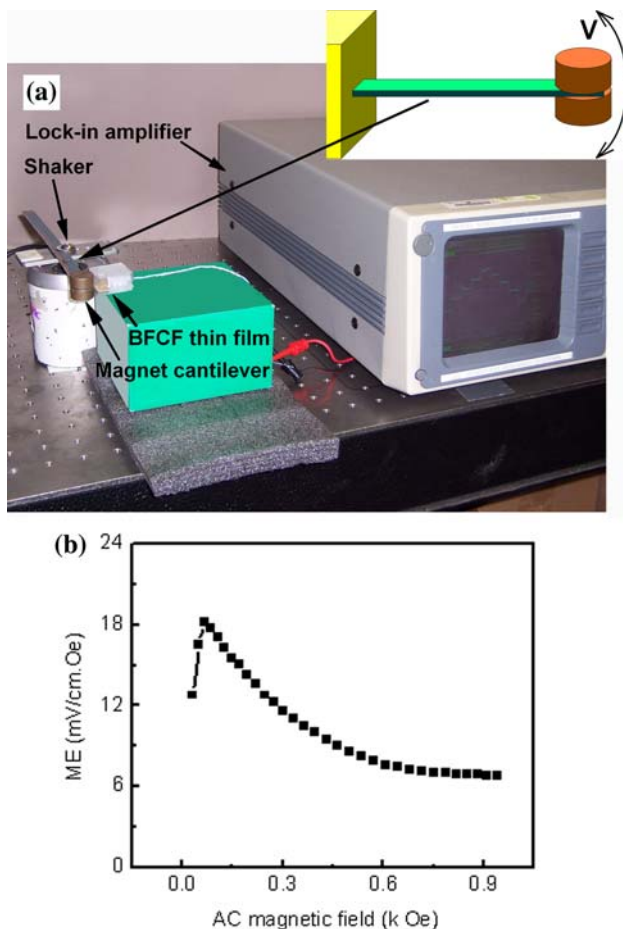


**Fig. 9** a Photo of our magnetic cantilever ME measurement method, where the inset is a schematic structure of the magnetic cantilever; and b the ME coefficient for a self-assembled BFO–CFO single-layered nano-composite thin film as a function of AC magnetic field amplitude [37]

magnet cantilever was controlled. The relationship between vibration amplitude and AC magnetic field was calibrated by using a Gaussmeter. This magnetic cantilever can generate an AC magnetic field up to 1 kOe. Using this method, the ME voltage output of self-assembled CFO–BFO can be higher than 1 mV.

The relationship between ME coefficient and AC magnetic field is shown in Fig. 9b. With increase of the AC magnetic field, the ME voltage coefficient increased quickly and reached 18 mV/cm Oe near 100 Oe. With further increase of the AC magnetic field, the ME coefficient dropped gradually to 6 mV/cm Oe at magnetic fields of above 1 kOe.

### Engineering of self-assembled two phase single grains, and complex composite geometries

Perovskite–spinel self-assembled epitaxial thin films have been deposited onto various substrates to improve their piezoelectric properties [89, 90]. But one disadvantage of thin films is that the substrate limits the distortion [5]. If one could transfer 2D BTO thin film structures onto other nanostructure without substrates, such as a self-assembly synthesis method to form two phase single grain particles, then novel performance might be enabled [91, 92].

Geometries of nano-composites controlled via compositional variations

To fabricate nano-composite grains, barium acetate, TiO<sub>2</sub>, MnO, ZnO, Fe<sub>2</sub>O<sub>3</sub>, NaCl, and NP-30 (nonylphenyl ether) were mixed with different molar ratios [93]. After mixing uniformly, they were annealed at 850 °C for 5 h. Here, we choose two representative final compositions for the two phase materials which correspond to: (i) (BaTiO<sub>3</sub>)<sub>2</sub>–Mn<sub>0.5</sub>Zn<sub>0.5</sub>Fe<sub>2</sub>O<sub>4</sub>, designated here as B<sub>2</sub>M<sub>1</sub>; and (ii) BaTiO<sub>3</sub>–(Mn<sub>0.5</sub>Zn<sub>0.5</sub>Fe<sub>2</sub>O<sub>4</sub>)<sub>2</sub>, designated here as B<sub>1</sub>M<sub>2</sub>.

Evidence of a change in the shape of particles for these different compounds was obtained by microscopy. In Fig. 10, we show grain morphologies for (a, b) pure MZF; (c, d) B<sub>1</sub>M<sub>2</sub>; (e, f) B<sub>2</sub>M<sub>1</sub>; and (g, h) pure BTO. The grains of BTO-rich samples had a rod-like morphology with a high aspect ratio and were approximately 200 nm in diameter, whereas the grains of the MZF-rich samples were octahedral-like and also approximately 200 nm in size. Both of them are similar to pure BTO and pure MZF, respectively. Here, the images in the left column of Fig. 10 were taken at low magnification and illustrate the ability to make such nanoparticles in larger quantities by solid state reaction, which is an advantage if compared with PLD. The images in the right column were obtained under much higher magnification and better illustrate how the grain geometries varied

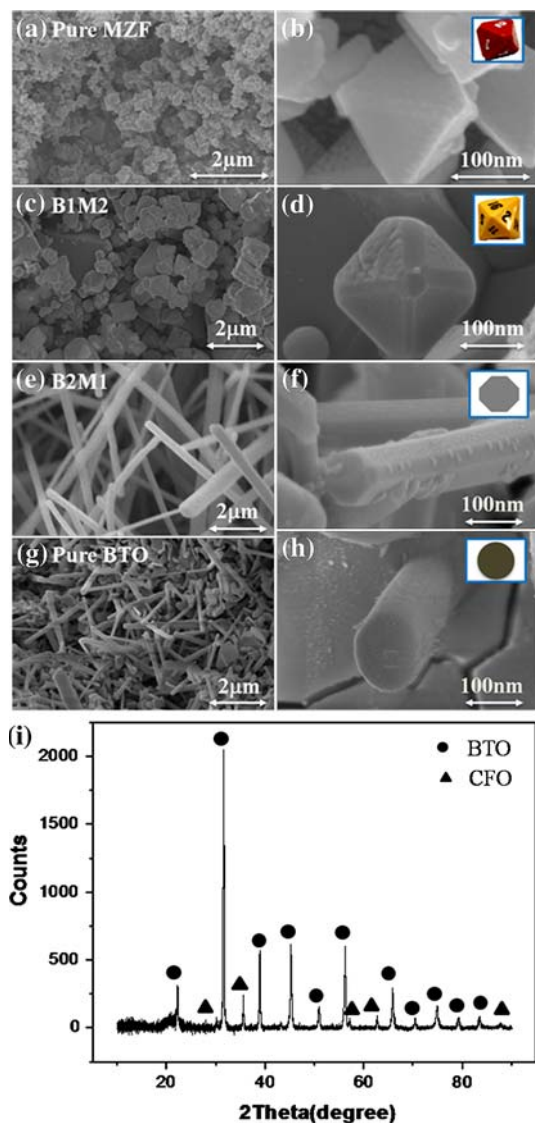


**Fig. 10** Scanning electron microscopy (SEM) images of **a, b** pure MZF nanoparticles; **c, d**  $\text{BTO}_1\text{-MZF}_2$  nanoparticles; **e, f**  $\text{BTO}_2\text{-MZF}_1$  nanorods; and **g, h** pure BTO nanorods, **(i)** XRD pattern measured from a sample shown in **(c)**. The inserts show schematics of the particle structures (**b** & **d**) and the cross-sectional geometries of the rods in images (**f** & **h**) [93]

with change in composition. Clearly, introduction of MZF into BTO changes the cross-sectional geometry, and alters the nanoparticles and nanorods' facets.

From high-resolution TEM images of the nanorods, as shown in Fig. 11a, we obtained a power spectrum from the Fourier transform of the area boxed-off in this lattice image, as shown in Fig. 11b. The power spectrum clearly reveals the presence of two sets of reflections. A HRTEM image was then taken at a higher magnification, as shown in Fig. 11c. At this higher magnification, we can see two regions, separated by a buffer zone approximately 1 nm in thickness, as marked in the figure. A BTO phase region is

identified whose inter-planar spacing was smaller than that of a MZF one. The lattice planes of the two phases were coherent, but yet in part elastically relaxed by the buffer zone. We obtained power spectrums from both the BTO and MZF phase regions of the lattice image, as shown in the inserts of Fig. 11c. Unlike that in Fig. 11b, these spectra each contained a single set of reflections, demonstrating that they were single phase BTO and MZF regions.

#### Geometries of nano-composites controlled via different oriented substrates

In addition to controlling the particle geometries by changing the compositional prescription, we also were able to control it via differently oriented substrates. In this case, we chose the BTO-rich prescription as a starting material and STO single crystals of different orientations as substrates. The control mechanism is expected to occur by heteroepitaxy and develop into facets through atomic rearrangements on a single crystal substrate with different orientations [94]. It is expected that the surface energy will change with orientation of the substrates due to variations in atomic arrangements. The facets and the final shape of nano-composites can then be defined by the anisotropy of the surface-energy, and be predicted by Wulff construction [95].

Different geometries of nanoparticles were observed on differently oriented substrates, as shown in Fig. 12 [96]. Compared with pure BTO or MZF, extra facets appeared for the  $\text{B}_2\text{M}_1$  composite. On (111) substrates, the particle morphology was triangular, similar to BTO perovskite when viewed along [111] (Fig. 12a) with (100), (001), and (010) facets. However, in our  $\text{B}_2\text{M}_1$  sample, three extra facets appeared on the particles that were not present for BTO grains. These are (101), (110), and (011) (Fig. 12b). In the larger  $\text{B}_2\text{M}_1$  particles, a seventh facet was also found along (111) as shown in Fig. 12c. A similar situation was found for (011) substrates, as shown Fig. 12f–h. On (001) substrates,  $\text{B}_2\text{M}_1$  particles were again found to have three additional facets: these are  $(\bar{1}12)$ , (112), and (001) as shown in Fig. 12j–l. Note that these additional facets are similar to those of MZF grains which have a pyramidal morphology as can be seen in Fig. 12i.

Next, we performed HRTEM investigations to better understand why these extra facets formed. Before doing so, we tilted our sample by  $45^\circ$ , so that we could observe the  $(0\bar{1}1)$  zone clearly below the (001) plane. Figure 13b shows a HRTEM image of the lift-out region where the dotted lines in part (a) schematically illustrate the lifted-out area. Part (c) is a SAED pattern, taken from the area of Fig. 13b. Note that we can observe a twofold splitting of the weaker spots near the STO ones, corresponding to an intimate two phase mixture in our  $\text{B}_2\text{M}_1$  layer, i.e., BTO

**Fig. 11** **a** High-resolution TEM image of our  $\text{BTO}_2\text{-MZF}_1$  nanorod; **b** power spectrum taken from a selected area of lattice image given in **(a)**; and **c** lattice image of higher resolution, demonstrating a buffer zone between phases, where the insets show power spectrums taken from the BTO and MZF areas, respectively [93]

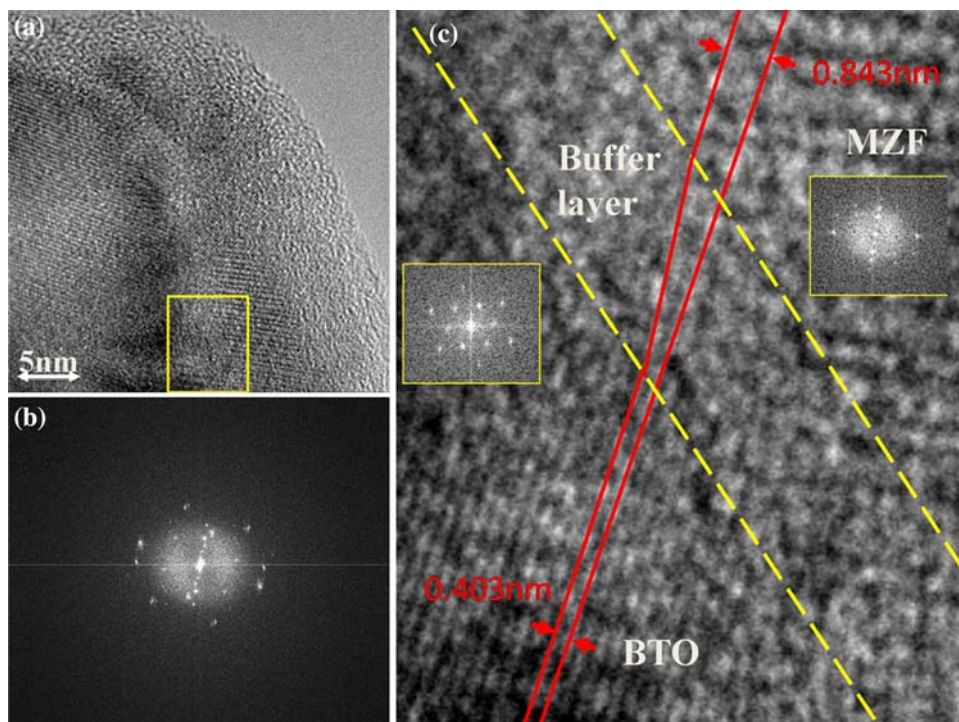
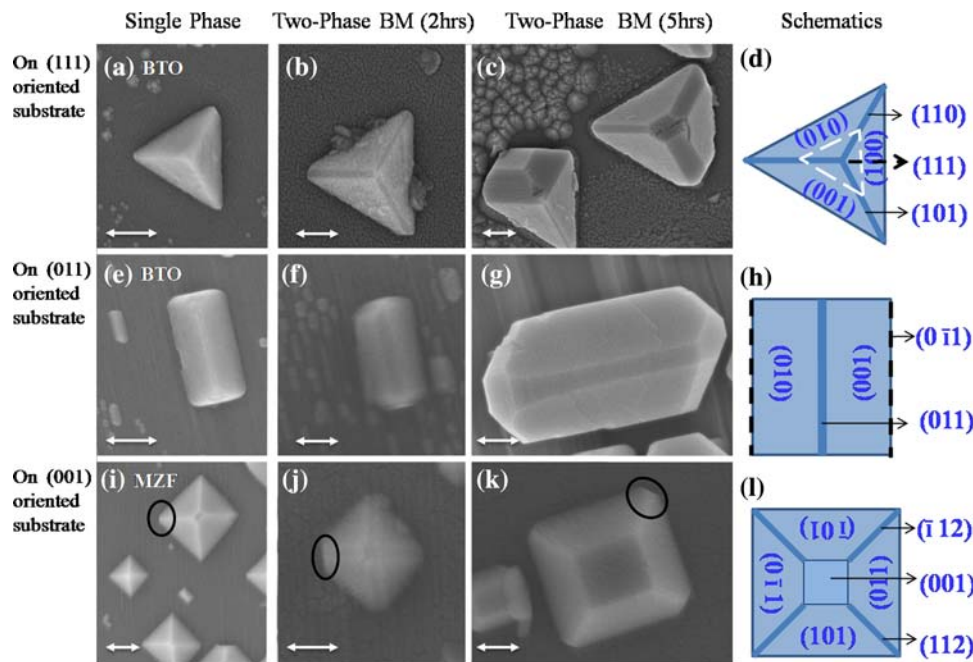


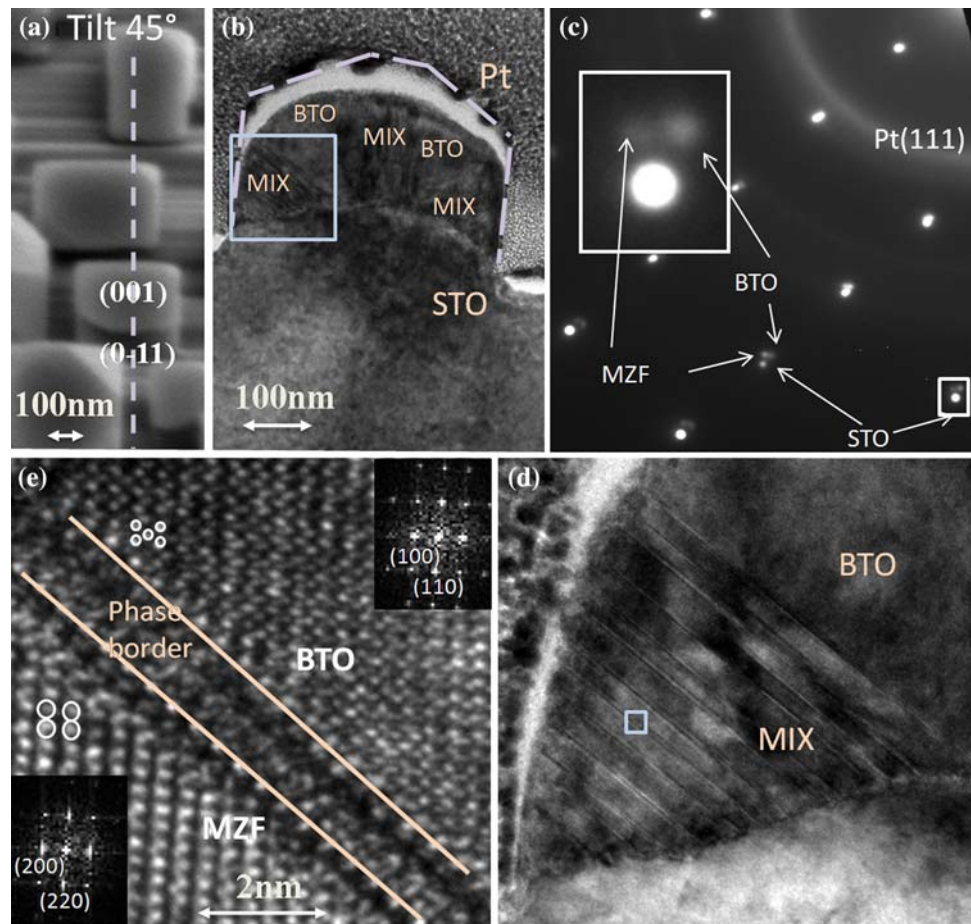
**Fig. 12** SEM images of  $\text{B}_2\text{M}_1$  nanoparticle and single phase samples. Same row is on same oriented STO substrates and same column is in same reaction condition. Following is the detailed information of each image: **(a, e)** are pure BTO nanostructures on (111) and (011) substrates; **(i)** is pure MZF on (001) substrate; **(b, f, and j)** are  $\text{B}_2\text{M}_1$  samples on (111), (011), and (001) substrates with short reaction time (2 h), respectively; **(c, g, and k)** are these  $\text{B}_2\text{M}_1$  samples made by increasing reaction time (5 h) on different substrates. All the scales are 200 nm, **(d, h, and l)** are schematics of marked facets of corresponding orientations in each row [96]



and MZF. These findings indicate that the two phases of the nano-composite grow epitaxially on each other. Parts (d) and (e) are two lattice images, where we zoom in from the light squares of the preceding images. We can see that the parallel streaks in (d) are actually transition layers. Our SAED pattern (Fig. 13c) revealed that BTO and MZF

phases coexist in this area. Here, two power spectra of these two lattices area provided additional evidence of phase coexistence and epitaxial growth, via a phase border (please see the inserts given in Fig. 13e). Clearly, two phases self-assembly occurred forming these nano-composites that grew into single grain particles.

**Fig. 13** (a) 45° tilted SEM image of the nano-composites grown on (011) oriented STO substrate. Dotted lines show schematically the FIB lifted-out area. (b) HRTEM image of the FIB lifted-out area. Dotted lines are the schematic diagram corresponding to dotted line in (a). (c) is SAED pattern taken from area shown in b. (d and e) are HRTEM images of corresponding areas marked in light squares from the previous magnifications. “BTO” here means only BaTiO<sub>3</sub> lattice area; “MIX” means BaTiO<sub>3</sub> and Mn<sub>0.5</sub>Zn<sub>0.5</sub>Fe<sub>2</sub>O<sub>4</sub> mixture area. Inserts in (e) are the power spectrum taken from two coexisted phases of (e) [96]



## Summary

We have reviewed various important recent developments in the field of multiferroic two-phase nano-composite thin films: with emphasis on our efforts to explore their new nano-structures, to understand their ferroelectric and ferromagnetic behaviors, and to improve their ME voltage output signals. Our review included the important findings, as follows: (i) nano-pillar, nano-maze, and nano-belt structures in perovskite–spinel systems that can be explained by a wetting model, an elastic model, and an anisotropic ledge growth mechanism for the CFO phase; (ii) the ferroelectric properties of composite thin films, which could be enhanced by epitaxial engineering using different oriented substrates; (iii) a strong magnetic anisotropy for nano-structure thin films, which is related to the constraint stress and aspect ratio of the ferrite phase of the nano-structure; (iv) the ME coupling between the piezoelectric and magnetostrictive phases as observed by several ways, such as a change in ferrite magnetization induced at the ferroelectric Curie temperature, a rotation of spin under weak magnetic fields that is assisted by electric fields, and the direct measurement of the ME voltage

output generated by AC magnetic fields; and (v) the nano-structures of two-phase nano-composite single grain particles with and without single crystal substrates.

**Acknowledgements** We gratefully acknowledge financial support from the U.S. Department of Energy under Contract No. DE-AC02-98CH10886, the Office of the Air-Force Office of Scientific Research under FA 9550-06-1-0410, and the National Science Foundation under DMR-0757502.

## References

- Schmid H (1994) *Ferroelectrics* 162:317
- Rado GT, Folen VJ (1961) *Phys Rev Lett* 7(8):310
- Folen VJ, Rado GT, Stalder EW (1961) *Phys Rev Lett* 6:607
- Wang J, Zheng H, Nagarajan V, Liu B, Ogale SB, Viehland D, Venugopalan V, Schlom DG, Wuttig M, Ramesh R, Neaton JB, Waghmare UV, Hill NA, Rabe KM (2003) *Science* 299:1719
- Zheng H, Wang J, Lofland SE, Ma Z, Mohaddes-Ardabili L, Zhao T, Salamanca-Riba L, Shinde SR, Ogale SB, Bai F, Viehland D, Jia Y, Ghlom DG, Wuttig M, Roytburd A, Ramesh R (2004) *Science* 303:661
- Wan JG, Wang XW, Wu YJ, Zeng M, Wang Y, Jiang H, Zhou WQ, Wang GH, Liu J-M (2005) *Appl Phys Lett* 86:122501
- Zhong XL, Wang JB, Liao M, Huang GJ, Xie SH, Zhou YC, Qiao Y, He JP (2007) *Appl Phys Lett* 90:152903

8. Liu M, Li X, Lou J, Zheng S, Du K, Sun NX (2007) *J Appl Phys* 102:083911
9. Ryu H, Murugavel P, Lee JH, Chae SC, Noh TW, Oh YS, Kim HJ, Kim KH, Jang JH, Kim M (2006) *Appl Phys Lett* 89:102907
10. Ren S, Wuttig M (2008) *Appl Phys Lett* 92:083502
11. Murakami M, Chang K-S, Aronova MA, Lin C-L, Yu MH, Hattrick-Simpers J, Wuttig M, Takeuchi I, Gao C, Hu B, Lofland SE, Knauss LA, Bendersky LA (2005) *Appl Phys Lett* 87:112901
12. Chang KS, Aronova MA, Lin CL, Murakami M, Yu MH, Hattrick-Simpers J, Famodu OO, Lee SY, Ramesh R, Wuttig M, Takeuchi I, Gao C, Bendersky LA (2004) *Appl Phys Lett* 84:3091
13. Deng C, Zhang Y, Ma J, Lin Y, Nan CW (2007) *J Appl Phys* 102:074114
14. Ryu S, Park JH, Jang HM (2007) *Appl Phys Lett* 91:142910
15. Ziese M, Bollero A, Panagiotopoulos I, Moutis N (2006) *Appl Phys Lett* 88:212502
16. He HC, Wang J, Zhou J-P, Nan C-W (2007) *Adv Funct Mater* 17:1333
17. He HC, Zhou JP, Wang J, Nan C-W (2006) *Appl Phys Lett* 89:052904
18. Zheng H, Zhan Q, Zavaliche F, Sherburne M, Straub F, Cruz MO, Chen LQ, Dahmen U, Ramesh R (2006) *Nano Lett* 6:1401
19. Zheng H, Straub F, Zhan Q, Yang PL, Hsieh WK, Zavaliche F, Chu YH, Dahmen U, Ramesh R (2006) *Adv Mater* 18:2747
20. Zavaliche F, Zheng H, Mohaddes-Ardabili L, Yang SY, Zhan Q, Shafer P, Reilly E, Chopdekar R, Jia Y, Wright P, Schlom DG, Suzuki Y, Ramesh R (2005) *Nano Lett* 5:1793
21. Zavaliche F, Zhao T, Zheng H, Straub F, Cruz MP, Yang P-L, Hao D, Ramesh R (2007) *Nano Lett* 7(6):1586
22. Levin I, Li J, Slutsker J, Roytburd AL (2006) *Adv Mater* 18:2044
23. Slutsker J, Tan Z, Roytburd AL, Levin I (2007) *J Mater Res* 22(8):2087
24. Zheng H, Wang J, Mohaddes-Ardabili L, Wuttig M, Salamanca-Riba L, Schlom DG, Ramesh R (2004) *Appl Phys Lett* 85:2035
25. Zhan Q, Yu R, Crane SP, Zheng H, Kisielowski C, Ramesh R (2006) *Appl Phys Lett* 89:172902
26. Li J, Levin I, Slutsker J, Provenzano V, Schenck PK, Ramesh R, Ouyang J, Roytburd AL (2005) *Appl Phys Lett* 87:072909
27. Levin I, Slutsker J, Li J, Tan Z, Roytburd AL (2007) *Appl Phys Lett* 91:062912
28. Ren S, Briber RM, Wuttig M (2008) *Appl Phys Lett* 93:173507
29. Muralidharan R, Dix N, Skumryev V, Varela M, Sanchez F, Fontcuberta J (2008) *J Appl Phys* 103:07E301
30. Zhang JX, Dai JY, Lu W, Chan HLW, Wu B, Li DX (2008) *J Phys D Appl Phys* 41:235405
31. Artemev A, Slutsker J, Roytburd AL (2005) *Acta Mater* 53:3425
32. Slutsker J, Levin I, Li J, Artemev A, Roytburd AL (2006) *Phys Rev B* 73:184127
33. Slutsker J, Roytburd A (2006) *Phase Transit* 79:1083
34. Yanina SV, Carter CB (2002) *Mater Res Soc Symp* 620:M9.4.1
35. Yan L, Li JF, Viehland D (2009) *Philos Mag*. doi:[10.1080/14786430902967702](https://doi.org/10.1080/14786430902967702)
36. Yan L, Bai FM, Li JF, Viehland D (2009) *J Am Ceram Soc* 92:17
37. Yan L, Xing Z, Wang Z, Wang T, Lei G, Li J, Viehland D (2009) *Appl Phys Lett* 94:192902
38. Speck JS, Selfert A, Pompe W, Ramesh R (1994) *J Appl Phys* 76:477
39. Lee J, Park G, Park C, Kim H (2006) *Appl Phys Lett* 88:072908
40. Hsu F, Leu C, Lu Y, Ho S, Hu C (2009) *J Am Ceram Soc* 92:389
41. Matthews JW, Blakeslee AE (1974) *J Cryst Growth* 27:118
42. People R, Bean JC (1985) *Appl Phys Lett* 47:322
43. Chen YB, Sun HP, Katz MB, Pan XQ, Choi KJ, Jang HW, Eom CB (2007) *Appl Phys Lett* 91:252906
44. Huang GF, Berger S (2003) *J Appl Phys* 93:2855
45. Alpay SP, Misirlioglu IB, Sharma A, Ban XG (2004) *J Appl Phys* 95:8118
46. Trithaveesak O, Schubert J, Buchal Ch (2005) *J Appl Phys* 98:114101
47. Petraru A, Pertsev NA, Kohlstedt H, Poppe U, Waser R, Solbach A, Klemradt U (2007) *J Appl Phys* 101:114106
48. Nagarajan V, Jenkins IG, Alpay SP, Li H, Aggarwal S, Salamanca-Riba L, Roytburd AL, Ramesh R (1999) *J Appl Phys* 86:595
49. Kim DM, Eom CB, Nagarajan V, Ouyang J, Ramesh R, Vait-hyananthan V, Schlom DG (2006) *Appl Phys Lett* 88:142904
50. Saito K, Ulyanenko A, Grossmann V, Röss H, Brüegemann L, Ohta H, Kurosawa T, Ueki S, Funakubo H (2006) *Jpn J Appl Phys* 45:7311
51. Speck JS, Daykin AC, Seifert A, Romanov AE, Pompe W (1995) *J Appl Phys* 78:1696
52. Alpay SP, Roytburd AL (1998) *J Appl Phys* 83:4714
53. Tuttle B, Headley T, Drewien C, Michael J, Voigt J, Garino T (1999) *Ferroelectrics* 221:209
54. Lee KS, Choi JH, Lee JY, Baik S (2001) *J Appl Phys* 90:4095
55. Choi KJ, Biegalski M, Li YL, Sharan A, Schubert J, Uecker R, Reiche P, Chen YB, Pan XQ, Gopalan V, Chen LQ, Schlom DG, Eom CB (2004) *Science* 306:1005
56. Jaffe B, Cook WR, Jaffe H (1971) *Piezoelectric ceramics*. Academic Press, New York, p 136
57. Noheda B, Cox DE, Shirane G, Gonzalo JA, Cross LE, Park SE (1999) *Appl Phys Lett* 74:2059
58. Yan L, Li JF, Cao H, Viehland D (2006) *Appl Phys Lett* 89:262905
59. Yokoyama S, Honda Y, Morioka H, Okamoto S, Funakubo H, Iijima T, Matsuda H, Saito K, Yamamoto T, Okino H, Sakata O, Kimura S (2005) *J Appl Phys* 98:094106
60. Smolenskii GA, Agranovskaya A, Popov SN, Isupov VA (1958) *Sov Phys Tech Phys* 28:2152 (in Russian)
61. Platonov GL, Drobyshev LA, Tomashpolskii YY, Venetsev YN (1970) *Sov Phys Crystallogr* 14:692
62. Bonny V, Bonin M, Sciau P, Schenk KJ, Chapuis G (1997) *Solid State Commun* 102:347
63. Vokov VA, Mylnikova IE, Smolenskii GA (1962) *Sov Phys JETP* 15:447
64. Yang Y, Liu JM, Huang HB, Zou WQ, Bao P, Liu ZG (2004) *Phys Rev B* 70:132101
65. Yang Y, Zhang ST, Huang HB, Chen YF, Liu ZG, Liu JM (2005) *Mater Lett* 59:1767
66. Ehses KH, Schmid H (1983) *Z Kristallogr* 162:64
67. Yan L, Li JF, Suchicital C, Viehland D (2006) *Appl Phys Lett* 89:132913
68. Yan L, Li JF, Viehland D (2008) *J Mater Res* 23:663
69. Yan L, Zhao X, Li JF, Viehland D (2009) *Appl Phys Lett* 94:192903
70. Kiselev SV, Ozerov RP, Zhdanov GS (1963) *Sov Phys Sokl* 7:742
71. Roginskaya YuE, Tomashpol'skii YuYa, Venetsev YuN, Petrov VM, Zhdanov G (1966) *Sov Phys JETP* 23:47
72. Smolenskii GA, Chupis I (1982) *Sov Phys Usp* 25(7):475
73. Venetsev YuN, Zhdanov G, Solov'ev S (1960) *Sov Phys Crystallogr* 4:538
74. Smolenskii GA, Isupov V, Agranovskaya A, Krainik N (1961) *Sov Phys Solid State* 2:2651
75. Fischer P, Polomska I, Sosnowska I, Szymanski M (1980) *J Phys C* 13:1931
76. Michel C, Moreau J-M, Achenbach GD, Gerson R, James WJ (1969) *Solid State Commun* 7:701
77. Bucci JD, Robertson BK, James WJ (1972) *J Appl Crystallogr* 5:187
78. Teague JR, Gerson R, James WJ (1970) *Solid State Commun* 8:1073
79. Sosnowska I, Perterlin-Neumaier T, Steichele E (1982) *J Phys C* 15:4835

80. Yan L, Cao H, Li JF, Viehland D (2009) *Appl Phys Lett* 94:132901
81. Xu G, Hiraka H, Shirane G, Li J, Wang J, Viehland D (2005) *Appl Phys Lett* 86:182905
82. Xu G, Li J, Viehland D (2006) *Appl Phys Lett* 89:222901
83. Zheng H, Kreisel J, Chu YH, Ramesh R, Salamanca-Riba L (2007) *Appl Phys Lett* 90:113113
84. Crane SP, Bihler C, Brandt MS, Goennenwein STB, Gajek M, Ramesh R (2009) *J Magn Magn Mater* 321:L5
85. Xing ZP, Li JF, Viehland D (2007) *Appl Phys Lett* 91:182902
86. Ortega N, Bhattacharya P, Katiyar RS, Dutta P, Manivannan A, Seehra MS, Takeuchi I, Majumder SB (2006) *J Appl Phys* 100:126105
87. Zhang JX, Dai JY, Chow CK, Sun CL, Lo VC, Chan HLW (2008) *Appl Phys Lett* 92:022901
88. Das J, Song YY, Mo N, Krivosik P, Patton CE (2009) *Adv Mater* 21:2045
89. Qiao L, Bi XF (2008) *J Cryst Growth* 310:5327
90. Yan L, Li JF, Viehland D (2007) *J Appl Phys* 101:104107
91. Yang YD, Qu LT, Dai LM, Kang TS, Durstock M (2007) *Adv Mater* 19:1239
92. Guo Z, Lee SE, Kim H, Park S, Hahn HT, Karki AB, Young DP (2009) *Acta Mater* 51:267
93. Yang YD, Li JF, Viehland D (2009) *J Am Ceram Soc.* doi: [10.1111/j.1551-2916.2009.03068.x](https://doi.org/10.1111/j.1551-2916.2009.03068.x)
94. Chen H, He Y, Shiflet GJ, Poon SJ (1994) *Nature* 367:541
95. Bodineau T, Ioffe D, Velenik Y (2000) *J Math Phys* 41:1033
96. Yang YD, Priya S, Wang YU, Li JF, Viehland D (2009) *J Mater Chem.* doi:[10.1039/b903762d](https://doi.org/10.1039/b903762d)